Macromolecules

pubs.acs.org/Macromolecules Article

Molecular Parameters Governing the Elastic Properties of Brush Particle Films

Jaejun Lee, Zongyu Wang, Jianan Zhang, Jiajun Yan, Tingwei Deng, Yuqi Zhao, Krzysztof Matyjaszewski, and Michael R. Bockstaller*

Cite This: *Macromolecules* 2020, 53, 1502−1513 Read Online

ACCESS | Metrics & More | Article Recommendations | Supporting Information

ABSTRACT: Elucidation of the mutual influence of composition and architecture of polymer canopies on the assembly and mechanical properties of brush particle-based materials holds the promise of advancing the understanding of the governing parameters controlling interactions in hybrid materials and the development of novel functional materials. In this work, the elastic properties of three series of brush particle systems were investigated, differentiated by grafting density as dense, intermediate, and sparse brush systems. Dense and intermediate systems displayed uniform microstructures; the degree of order (measured using Voronoi cell area analysis) increased with grafting density. For dense and intermediate brush particle systems, instrumented indentation analysis revealed an increase of the elastic modulus with the degree of polymerization of tethered chains, in contrast to effective medium predictions. Furthermore, the contribution of ligands to particle interactions increased with decreasing grafting density. The results indicated that the response behavior of particle brush films in tensile-type deformations depends on dispersion interactions between ligands of adjacent brush particles. The more pronounced brush interdigitation in the case of intermediate graft densities enhanced the dispersion interactions between brush particles and hence the modulus of films. A reversed trend in modulus was observed in films of sparse brush particles that also featured the formation of string-like superstructures. Here, the elastic modulus was substantially increased for low-molecular ligands and continuously decreased with increasing degree of polymerization of tethered chains along with a transition from string-like to uniform morphologies. Independent of grafting density, the elastic modulus of the pristine polymer was recovered in the limit of a high degree of polymerization of polymer ligands.

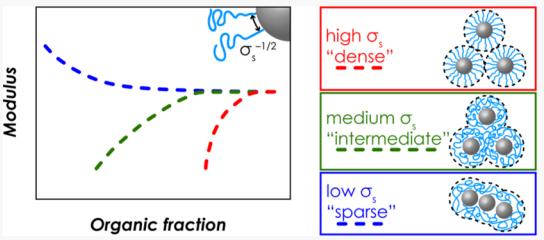

INTRODUCTION

Recent advances in the field of surface-initiated reversible deactivation radical polymerization enable the grafting of polymeric chains to the surface of nanoparticles (NPs) with controlled grafting density, molecular weight, dispersity, and composition.[1−7] The resulting brush (or "hairy") particles have been pursued as building blocks for the fabrication of "one-component hybrid materials" that are formed via the assembly of brush particles in the absence of an additional matrix polymer.[8−14] Interest in one-component hybrids is motivated by microstructural features that give rise to novel property characteristics.[15,16] Mean-field theory, computer simulations, and experiments have revealed that "steric confinement" in sufficiently dense brush materials gives rise to a transition of chain conformation from more stretched (in the vicinity of the surface) to more relaxed at sufficiently high degree of polymerization or low grafting density or small particle size.[7−9,11,13,16−23] Because physical properties of polymers are sensitive to orientation, this presents the prospect of realizing novel functionalities in brush particle hybrids by deliberate control of the orientation of tethered chains. For example, increasing chain orientation in dense brush systems has been argued to raise thermal transport, to reduce dielectric breakdown, or to result in novel phonon transport characteristics of brush particle hybrids.[25−27] More relaxed (coiled) chain conformations were shown to promote chain entanglement, thus giving rise to polymer-like deformation properties and formability.[8−10] This was used to enable the fabrication of "moldable colloidal crystals" as well as transparent high refractive index glasses or low-modulus hybrid elastomers that might find use in soft robotics.[9,13,28−30] As brush particles are assembled into films (these will be denoted "particle solids" in the following), the constraints arising from the packing into ordered structures have been shown to induce further chain perturbation that has been harnessed; for example, for the fabrication of mesoporous membranes.[31]

As the density of tethered chains is reduced to values of about 0.05 nm^{-2} (the so-called "sparse" grafting regime), distinctive differences in the assembly behavior of brush particles—such as the formation of anisotropic sheet and string

Received: August 28, 2019
Revised: December 29, 2019
Published: February 3, 2020

https://dx.doi.org/10.1021/acs.macromol.9b01809
Macromolecules 2020, 53, 1502−1513

structures—was observed.[14,19,24,32−38] The polarization of particle interactions was related to the segregation of tethered chains into the galley regions between particle strings. This breaking of symmetry is thought to minimize free energy by enabling more relaxed chain conformations and more effective particle core interactions.[32−36]

To understand the effect of brush architecture on material performance, research has focused on the thermomechanical and relaxation behavior of brush particle hybrids. With regard to mechanical properties of solid brush particle films, two quantities were of particular interest, that is, the elastic (Young) modulus and the fracture toughness.[39−41] The former is related to short-range interactions between constituents (and thus gives information about the relevant bonding interactions), while the latter gives insight into dissipative pathways within materials during fracture. Elasticity of particle brush solids was evaluated using a variety of techniques such as microindentation and nanoindentation, uniaxial extension, buckling, and non-contact Brillouin scattering.[8,9,24,27,32,42−46] Indentation experiments by Podsiadlo et al. (on films assembled from low-molecular surfactant-coated semiconductor nanocrystals) were the first to suggest that the elastic response of particle solids is determined by dispersion interactions between tethered ligands.[42] Nanoindentation in conjunction with tensile testing confirmed this conclusion for polymeric ligands.[8,9,24,46,47] These studies further revealed a toughening transition above a threshold molecular weight of polymeric tethers that was attributed to the onset of entanglement of tethered chains and the associated increase in ductility of particle brush hybrids. Experiments, theory, and simulations correlated this brittle−ductile transition to the more relaxed (coiled) chain conformations that are favored for sufficiently large degree of polymerization.[8,20,22,23,48] In sparse grafted systems, mechanical analysis (using wrinkling and shear tests) have revealed a significant enhancement of elastic moduli.[24,32] This was interpreted to be a consequence of the organization of sparse brush particles into anisotropic string-like superstructures. Recent BLS experiments and simulations suggested that this "strengthening effect" is caused by the concentration of polymer segments within "interstitial spaces" between particle strings and the associated increase of the contribution of core−core interactions to the elastic modulus.[20,45]

Collectively, previous research illustrates the relevance of brush architecture on the properties of particle brush-based materials. A requisite for translating these results into opportunities for material design is the better understanding of the mutual influence of the various relevant characteristics of polymer canopies on performance. For example, while in the case of densely grafted particles, the modulus and toughness have been shown to increase with molecular weight of polymeric tethers; the associated reduction of the inorganic content limits the practical use of the one-component hybrid approach for material design.[8−10,47] A concurrent reduction of the grafting density could alleviate this problem. This raises intriguing questions: is there an optimum graft density to enhance mechanical properties of particle brush materials? Can isotropic microstructures be retained in the limit of low grafting densities (which might be preferable for some applications)? What is the role of graft composition (monomodal vs multimodal) and chain dispersity (narrow vs wide) on the interactions in brush particle materials? This contribution presents a systematic evaluation of the effect of grafting density on the structure and elastic properties of narrow-dispersed and monomodal brush particle systems; the role of graft molecular weight distribution (MWD) will be explored in a subsequent paper. Six series of particle brush model systems representing the dense, intermediate, and sparse grafting regimes, respectively, were evaluated. In principle, the distinct grafting regimes could be distinguished on the basis of the conformation of tethered chains that is predicted, for example, via the Daoud−Cotton model.[49−52] The latter ascribes a "critical" radius $r_c = r_0\sigma_s^{1/2}/\nu$, where σ_s denotes the grafting density, r_0 denotes the particle radius, and ν denotes the excluded volume parameter, to indicate the transition between two conformational regimes. Segmental crowding in the limit of $r < r_c$ is predicted to induce stretched chain conformations (the concentrated polymer brush regime, CPB), whereas relaxed conformations are expected for a brush particle diameter $r > r_c$ (the semidilute polymer brush regime, SDPB). Conceptually, one might then distinguish dense, intermediate, and sparse grafting regimes, as those corresponding to $r_0 < r_c$, $r_0 \approx r_c$, and $r_0 > r_c$, respectively. However, in the literature, the sparse grafting regime has been often identified on an empirical basis as the regime in which grafting density is low enough to drive the formation of string-like superstructures.[33] The latter not only depends on the characteristics of tethered chains but also on geometrical features such as particle size or uniformity.[23,32] For this reason, in the following, a more "ad hoc" definition of grafting regimes will be adopted that is based on the underlying initiator density and the observed behavior of brush particle assemblies. The material systems consist of silica particles with radius $r_0 = 7.9 \pm 2.2$ nm tethered with polystyrene (PS) and poly(methyl methacrylate) (PMMA). Both polymers are glassy at room temperature for all tested molecular weights. This is a requisite for the purpose of the present study as it simplifies the analysis of elastic properties and avoids convoluting influences of morphological features (such as semicrystallinity) on structure−property relations. Dense, intermediate, and sparse regimes are defined as grafting density in the range of 1, 0.3, and 0.05 nm^{-2} (the numbers correspond to the respective density of initiator sites, see below). While this definition is, by nature, specific for the present material system, the conclusions are consistent with reported findings in the literature on diverse brush particle compositions.[9,24] We thus expect this classification to be useful as a basis for the more general categorization of brush particle systems. For brush particles with dense and intermediate grafting density, we find the contribution of ligands to particle interactions (measured in terms of the change of Young's modulus per volume fraction of polymer repeat units) to increase with decreasing grafting density. This trend is in contrast to effective medium predictions and interpreted to be a consequence of increased brush interdigitation which increases interactions between ligands of adjacent particles and thus the resistance to tensile-type deformation. In this regime, the elastic modulus increases with the degree of polymerization of tethered chains, a trend that is captured by a model that attributes the effective brush particle interactions to the dispersion forces between segments of interdigitated chains. In contrast, the opposite trend in modulus is observed in films of sparse brush particles that feature the formation of string-like superstructures. Our results point to subtle relationships between brush architecture, interactions, and properties of brush particle films that could benefit material design and hence merit further investigation.

https://dx.doi.org/10.1021/acs.macromol.9b01809
Macromolecules 2020, 53, 1502−1513

RESULTS AND DISCUSSION

A library of silica particle (r_0 = 7.9 ± 2.2 nm) brush materials with systematically varied degrees of polymerization (N) of grafted PS and PMMA chains as well as surface grafting density (σ_s) was synthesized via surface-initiated atom-transfer radical polymerization (SI-ATRP) using established protocols.[1,3,5,53,54] The classification of brush particles into dense, intermediate, and sparse [sample ID: SiO_2-d/i/s-(S or methyl methacrylate (MMA))N] is based on the respective composition of active and inactive sites of partially passivated silica particles as illustrated in Figure 1.

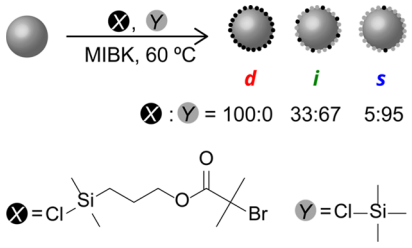

Figure 1. Synthesis and categorization of dense (d), intermediate (i), and sparse (s) brush particles. Control of grafting density is facilitated by silanization with a distinct ratio between active initiator (X, black circle; 3-(chlorodimethylsilyl)propyl 2-bromoisobutyrate, BiBSiCl) and inactive (Y, gray circle; chlorotrimethylsilane) sites.

A summary of the relevant characteristics of PS and PMMA brush particle systems is presented in Tables 1 and 2. Where possible, the results will be complemented with those of PMMA brush particles (~0.4 chains/nm^2) that were synthesized as part of a previous study (and hence present an independent reference) to highlight the generalizability of the presented results. The compositional characteristics for these particles are tabulated in Table S1; data relating to these materials in figures are marked with asterisks.

The structure of particle brush materials was characterized using transmission electron microscopy (TEM). Figures 2 (and S1) display representative TEM images of PS (PMMA) brush materials in the respective grafting regime. Brush particles in the dense and intermediate grafting regimes displayed uniform microstructures while sparse systems displayed the formation of string-like superstructures. To determine whether uniform or string-like structures were present, image analysis was performed on electron micrographs on particle monolayers (after vacuum annealing at T = 130 °C, 24 h) to determine the distance between adjacent particles. Structures were considered "uniform" if distance distributions were monomodal; in this case, the average distance was denoted d. In contrast, structures were considered "string-like" if a bimodal distribution of particle distances was observed (Figures S3 and S4 depict examples of the analysis for the images shown in Figure 2a–c). For dense and intermediate grafting densities, Voronoi cell analysis revealed that the degree of ordering (measured in terms of the variance of Voronoi cell area, see insets of Figure 2a,b and similar Figure S1 for PMMA systems) in particle brush films decreases with grafting density. Following procedures established in the literature, a measure for the "degree of order" was defined as 1 − fwhm where fwhm is the full-width at half-maximum of the distribution of Voronoi cell areas, normalized by the average cell area.[47] Figure 2d displays 1 − fwhm of PS-brush systems clearly revealing the trend toward a higher degree of structural order

Table 1. Molecular Characteristics of PS-Tethered SiO_2-d/i/s-SN Brush Particles[a]

sample ID	N	M_w/M_n	f_{org}	ϕ_{org}	σ_s (nm^{-2})
SiO_2-d-S120	120	1.17	0.75	0.86	0.78
SiO_2-d-S136	136	1.11	0.78	0.88	0.85
SiO_2-d-S204	204	1.10	0.83	0.91	0.74
SiO_2-d-S212	212	1.14	0.83	0.91	0.72
SiO_2-d-S226	226	1.11	0.84	0.92	0.74
SiO_2-d-S231	231	1.20	0.82	0.90	0.62
SiO_2-d-S231(2)	231	1.14	0.85	0.92	0.78
SiO_2-d-S355	355	1.10	0.87	0.94	0.61
SiO_2-d-S365	365	1.15	0.89	0.94	0.71
SiO_2-d-S365(2)	365	1.18	0.87	0.93	0.58
SiO_2-d-S400	400	1.22	0.88	0.94	0.61
SiO_2-d-S432	432	1.47	0.91	0.96	0.75
SiO_2-d-S549	549	1.25	0.89	0.94	0.46
SiO_2-d-S638	638	1.36	0.91	0.95	0.50
SiO_2-d-S762	762	1.35	0.92	0.96	0.49
SiO_2-d-S829	829	1.72	0.94	0.97	0.60
SiO_2-d-S841	841	1.18	0.93	0.96	0.48
SiO_2-d-S890	890	1.25	0.93	0.96	0.45
SiO_2-d-S1087	1087	1.28	0.92	0.96	0.33
SiO_2-d-S1777	1777	1.19	0.91	0.96	0.19
SiO_2-d-S1800	1800	1.42	0.93	0.96	0.22
SiO_2-i-S221	221	1.09	0.55	0.72	0.17
SiO_2-i-S255	255	1.11	0.49	0.66	0.12
SiO_2-i-S313	313	1.15	0.59	0.75	0.15
SiO_2-i-S328	328	1.14	0.62	0.77	0.16
SiO_2-i-S440	440	1.15	0.63	0.78	0.12
SiO_2-i-S758	758	1.10	0.71	0.84	0.10
SiO_2-i-S1103	1103	1.24	0.72	0.84	0.07
SiO_2-s-S432	432	1.21	0.31	0.48	0.03
SiO_2-s-S600	600	1.29	0.42	0.60	0.04
SiO_2-s-S954	954	1.33	0.45	0.63	0.03
SiO_2-s-S1576	1576	1.47	0.55	0.72	0.03

[a]Variables represent the degree of the polymerization of graft, N; dispersity index, M_w/M_n; weight fraction of polymer, f_{org}; volume fraction of polymer, ϕ_{org}; surface grafting density, σ_s.

in films of dense brush systems. This is attributed to the more hard-sphere-type interaction potential in dense brush particle systems that support the formation of more ordered structures.[2,47,52,55−58]

In agreement with literature reports, sparsely grafted systems were found to form string-like superstructures (the conclusion of string vs sheet structures was based on imaging microsectioned bulk materials, as shown in Figure S5).[14,21,23,32,34,59,60] Hence, while dense and intermediate brush particle assemblies were described by one characteristic distance d, sparse systems were characterized by two distances that will in the following be denoted d (representing the interstring particle distance) and d' (representing the intrastring particle distance; see also Figure S3). The interstring distance was considered as the analogue to d in dense/intermediate systems because it identifies the spacing between particles separated by polymeric ligands. The average number of particles per string of SiO_2-s-S432 determined from Figure 2c was approximately 23. Strings were identified as a group of particles separated by a distance less than 5 nm (because d' was found to be less than this value, see Figure S3c). A representative micrograph illustrating string identification is shown in Figure S4. It is noted that while recent simulation

https://dx.doi.org/10.1021/acs.macromol.9b01809
Macromolecules 2020, 53, 1502−1513

Table 2. Molecular Characteristics of PMMA-Tethered SiO_2-d/i/s-MMA*N* Brush Particles[a]

sample ID	N	M_w/M_n	f_{org}	ϕ_{org}	σ_s (nm^{-2})
SiO_2-d-MMA188	188	1.21	0.80	0.88	0.71
SiO_2-d-MMA213	213	1.18	0.82	0.90	0.69
SiO_2-d-MMA250	250	1.25	0.84	0.91	0.69
SiO_2-d-MMA382	382	1.15	0.90	0.95	0.79
SiO_2-d-MMA405	405	1.18	0.89	0.94	0.68
SiO_2-d-MMA445	445	1.16	0.91	0.95	0.76
SiO_2-d-MMA460	460	1.18	0.92	0.96	0.80
SiO_2-d-MMA777	777	1.15	0.95	0.97	0.78
SiO_2-i-MMA206	206	1.35	0.49	0.65	0.16
SiO_2-i-MMA379	379	1.22	0.70	0.82	0.20
SiO_2-i-MMA563	563	1.13	0.74	0.84	0.17
SiO_2-i-MMA637	637	1.25	0.78	0.87	0.19
SiO_2-i-MMA732	732	1.13	0.83	0.90	0.22
SiO_2-i-MMA752	752	1.24	0.83	0.90	0.21
SiO_2-s-MMA232	232	1.23	0.23	0.36	0.04
SiO_2-s-MMA365	365	1.15	0.32	0.47	0.04
SiO_2-s-MMA401	401	1.17	0.38	0.54	0.05
SiO_2-s-MMA477	477	1.13	0.42	0.58	0.05
SiO_2-s-MMA798	798	1.07	0.53	0.68	0.05
SiO_2-s-MMA993	993	1.11	0.62	0.75	0.05
SiO_2-s-MMA1067	1067	1.25	0.65	0.78	0.06
SiO_2-s-MMA1147	1147	1.27	0.64	0.78	0.05
SiO_2-s-MMA1410	1410	1.11	0.70	0.82	0.05

[a]Variables represent the degree of polymerization of graft, N; dispersity index, M_w/M_n; weight fraction of polymer, f_{org}; volume fraction of polymer, ϕ_{org}; surface grafting density, σ_s.

studies have suggested transitions from string to sheet-type morphologies to occur depending on the length of tethered chains, no such transitions were observed in the present case. This might be attributed to the effect of particle size dispersity and compositional heterogeneity that was not accounted for in simulations.[37,61] The structure formation of sparse systems will be discussed in more detail in the later part of this paper.

To discern the effect of grafting density on the conformation of tethered chains, the characteristic distance d was analyzed by electron imaging. Figure 3 displays the dependence of

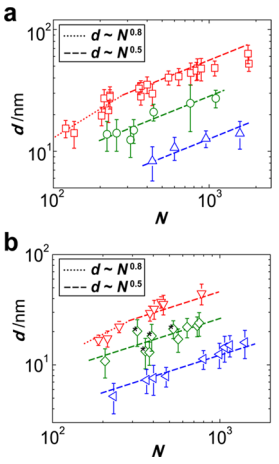

Figure 3. Dependence of the characteristic distance d (dense and intermediate: interparticle distance, sparse: interstring distance) on the degree of polymerization of PS (a) or PMMA (b) for all systems (red: dense, green: intermediate and blue: sparse system). The trend lines indicate corresponding brush regimes: CPB (dotted) and SDPB (dashed). Data points with asterisks indicate additional (intermediate dense) PMMA brush particles.

interparticle distance on N for brush particles in the various grafting regimes. Dense brush systems (red symbols) reveal two distinct regimes with scaling exponents 0.8 and 0.5, thus indicating a transition from oriented to random chain conformation with an increasing degree of polymerization. This supports previous findings on dense brush particle systems that were analyzed using TEM and scattering analysis.[9,47,58,62,63] The transition between the two regimes occurs at a similar degree of polymerization ($N_{crit} \approx 300$) for PS and PMMA brush particles. This finding is attributed to the similar grafting density and comparable persistence length of

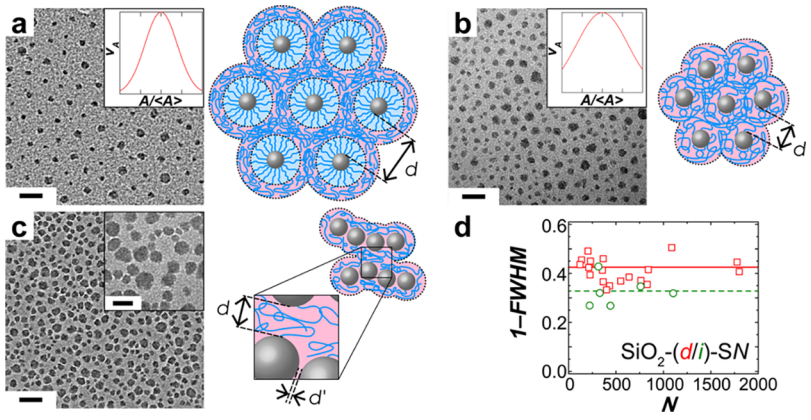

Figure 2. Representative bright-field transmission electron micrographs for (a) dense (SiO_2-d-S365), (b) intermediate (SiO_2-i-S328), and (c) sparse (SiO_2-s-S432) PS-brush systems with similar degrees of polymerization. Also shown are schematic illustrations of the corresponding microstructures. The characteristic distance d is defined as interparticle distance in dense and intermediate systems and as interstring distance in the sparse system. The area distributions of the Voronoi cell from the dense and the intermediate materials are shown as insets in (a,b). All scale bars are 50 nm (20 nm in insets). (d) Comparison of 1 − fwhm for monolayer particle brush films of dense (red circles) and intermediate (green squares) systems. Larger values indicate a higher degree of order (for the case of a close packing of spheres in a plane, a reference value of "1" is expected). For dense and intermediate brush systems, an average degree of order $\langle 1 - \text{fwhm}\rangle_{dense} = 0.422$ and $\langle 1 - \text{fwhm}\rangle_{interm.} = 0.325$ is observed (indicated by red solid and green dashed lines, respectively).

https://dx.doi.org/10.1021/acs.macromol.9b01809
Macromolecules 2020, 53, 1502−1513

both polymers.[50] In contrast, intermediate brush systems (green symbols) as well as the interstring distance in the case of sparse brush particles (blue symbols) exhibit $N^{0.5}$ scaling for all (tested) values of N. This is consistent with the expectation that a reduction of chain crowding across the particle surface affords more relaxed chain conformations. For the case of sparse brush particle systems, we note that the $N^{0.5}$ scaling supports prior reports that attributed the formation of string structures in part to the increase of chain conformational entropy that is associated with the segregation of polymer chains to the galley regions between particle strings.[24,32,34] We also note that no effect of N on the intrastring distance d' was observed; however, the average "length" of strings decreased with increasing N (this aspect will be further discussed below). Interestingly, the distances measured in particle monolayers for dense and intermediate brush particle systems were in good agreement with those estimated based on the inorganic content of the respective materials (see Figure S6).[64,65] In contrast, the assumption of a uniform microstructure results in the under estimation of d for sparse particle systems, thus providing further evidence for the formation of anisotropic superstructures.

The elastic modulus (E) and hardness (H) of 20−60 μm thick brush particle films were measured using nanoindentation after thermal annealing in vacuum (T = 130 °C, 24 h). Representative load−displacement curves and images of residual indents are shown in Figure S7. Measurements were recorded at a displacement rate of 5 nm/s. Variation of the indentation rate in the range 1−25 nm/s was used to confirm the absence of viscoelastic contributions to the response of films.[8] This is important because our analysis of instrumented indentation results rests on the assumption of samples undergoing elastic−plastic deformation only. Indentation depths of 500 nm were chosen to ensure meaningful sampling of interactions (the test volume 20 μm^3 corresponds to >1,000 brush particles). The elastic modulus was evaluated from load−displacement curves using the Oliver−Pharr method that has been shown to yield results with satisfying accuracy for glassy polymeric materials.[66] Films were imaged [using atomic force microscopy (AFM)] after indentation to ensure the absence of excessive pile-up in the indent region (Figure S7). For each sample, more than nine independent measurements were evaluated. Figure 4 depicts the resulting trends of E and H along with the respective standard deviations. While discussing the results, we will focus on the elastic modulus because it directly relates to constituent interactions in materials. It should be noted that the determination of E from indentation analysis requires knowledge of the materials' Poisson ratio. The latter was estimated on the basis of effective medium theory. To support the validity of this analysis, we also show the corresponding trend in sample hardness. The latter is directly obtained from indentation analysis without assumption of other material parameters. The common trend of E and H that is seen for all systems in Figure 4 supports the validity of the analysis.

The elastic moduli (and hardness) of bare and initiator-tethered silica particle films were measured as a reference. The elastic modulus of initiated-tethered reference systems was determined to be 1.8 GPa (black symbols in Figure 4), regardless of the ratio of the active initiator to inactive sites. We note that the total modification density (active and inactive sites) was identical for d/i/s—brush systems (~1 nm^{-2}); only the ratio of active and inactive surface groups changed

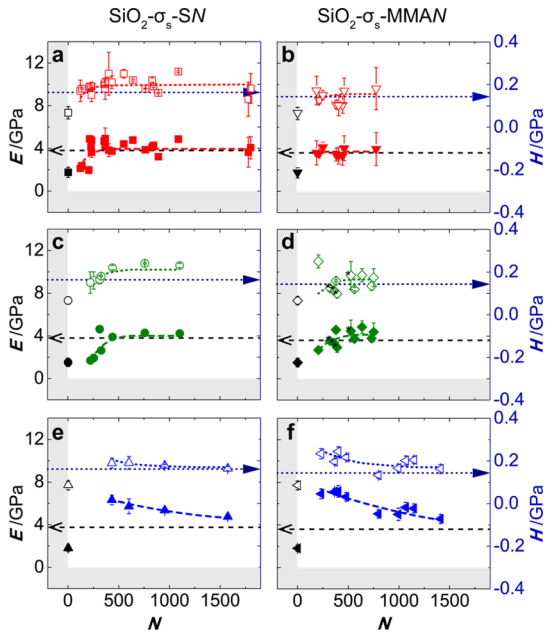

Figure 4. Young's modulus (E, left y-axes, filled symbols) and hardness (H, right y-axes, open symbols) of PS-grafted (left column) and PMMA-grafted (right column) particle films in the (a,b) dense, (c,d) intermediate, and (e,f) sparse systems measured by nanoindentation. Fitted lines from the data are exhibited as dotted (for H) and dashed (for E) lines with the same colors. The black and navy dashed lines indicate the elastic modulus and hardness (E_{PS} = 3.9 GPa, E_{PMMA} = 3.8 GPa, H_{PS} = 0.16 GPa, H_{PMMA} = 0.14 GPa) of bulk homopolymer reference systems with degree of polymerization N_{PS} = 500 and N_{PMMA} = 1200. The data points at N = 1 (black symbols) correspond to initiator-tethered NP films. Axis labels and titles in the intervening spaces are removed for convenience.

accordingly for the different systems. This value was markedly less than the value (5.5 GPa) measured for pristine hydroxy-functionalized silica particles. This result confirmed a previous report on the effect of organic ligand coatings on silica particle interactions and was rationalized as a consequence of the weaker cohesive interactions upon replacement of polar hydroxy-group functionalities with nonpolar low-molecular ligands (trichlorosilane or initiator) that interact predominantly through dispersion interactions.[42,67,68] The result thus further supported the conclusion that brush particle interactions are dominated by ligand−ligand rather than core−core interactions. Increasing the degree of polymerization of tethered chains was found to exert two distinct effects, depending on the grafting density. For brush systems with dense and intermediate grafting density (Figures 4a−d), the elastic modulus (and hardness) continuously increased and eventually leveled off at values similar to the respective bulk homopolymer reference (E_{PS} = 3.9 GPa and E_{PMMA} = 3.8 GPa) which are indicated as dotted lines in Figure 4. We rationalized the threshold degree of polymerization for leveling-off as being related to a correlation length beyond which dispersion interactions become independent of chain length (an analogous argument applies to the molecular weight dependence of the elastic modulus of amorphous polymers[39]).

In stark contrast to dense and intermediate systems, sparse brush particle films displayed an opposite behavior (Figure 4e,f). Here, the elastic modulus assumed a maximum value for the smallest N tested (6.3 GPa for PS with N = 432 and 6.9 GPa for PMMA with N = 232) and subsequently decreased

https://dx.doi.org/10.1021/acs.macromol.9b01809
Macromolecules 2020, 53, 1502−1513

with increasing degree of polymerization. This trend was rationalized as a consequence of the anisotropic assembly structures in sparse brush particle films (see below).

To evaluate the role of graft architecture on the elastic modulus in dense and intermediate brush particle systems, Figure 5 depicts the dependence of E on the organic volume fraction ϕ_{org} for the case of PS brush particles. Interestingly, the elastic modulus of intermediate brush systems increased at a distinctively lower threshold volume fraction of the polymer component. Conversely, at equal volume fraction of the organic component, the elastic modulus of intermediate brush systems systematically exceeded the modulus of dense analogues. For example, sample SiO_2-i-S1103 (indicated by the green arrow in Figure 5) exhibited a modulus of E = 4.2 GPa, while the dense analogue, SiO_2-d-S120 (indicated by the red arrow in Figure 5) only displayed E = 2.1 GPa. The data thus revealed polymer repeat units to be more effective in raising brush interactions in the case of intermediate brush architectures.

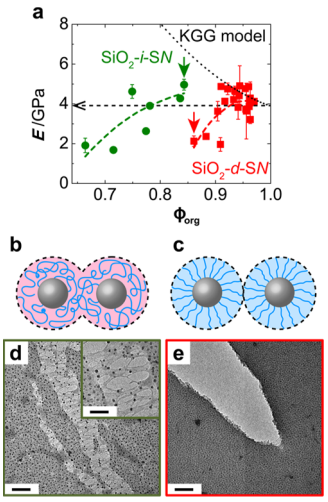

Figure 5. (a) Young's moduli of the dense (red squares) and intermediate (green circles) PS-grafted particle films as a function of the volume fraction of the polymer with trend lines. The black dashed line indicates the elastic modulus of bulk homopolymer reference (E_{PS} = 3.9 GPa). Arrows indicate systems with comparable composition (green: SiO_2-i-S1103, red: SiO_2-d-S120) that were chosen for crack formation analysis. Dotted line indicates effective medium prediction (Kuhn–Guth–Gold model).[69] The panel (b,c) illustrates chain structures of intermediate (b) and dense (c) systems. The panel (d,e) show TEM micrographs of SiO_2-i-S1103 and SiO_2-d-S120. The inset in the panel (d) is a magnified micrograph showing craze formation. Scale bars are 200 nm (100 nm in the inset).

It is noted that the trend shown in Figure 5a is in contrast to the effective medium prediction (dotted line in Figure 5a) that predicts the elastic modulus to increase with the inorganic content (i.e., with decreasing degree of polymerization of tethered chains). To rationalize this observation, we proposed that the relevant component of the total cohesive interactions with regard to the measured elastic modulus in instrumented indentation analysis—at least in the case of dense and intermediate systems—is the dispersion interaction between ligands of adjacent particles. The latter should be sensitive to the interdigitation of brush layers between adjacent particles. We note that because of the pronounced distance dependence of dispersion interactions [$U(r) \approx r^{-6}$, where r is the distance between two molecules] "side-on" orientation of ligands should contribute substantially more to the net bonding interactions as compared to "end-on" alignment.[70] The reduced elastic modulus of dense brush systems could thus be interpreted as a consequence of the reduction of cohesive interactions in non-interdigitating brush particle assemblies. This situation is schematically depicted in Figure 5b,c. Indirect evidence for the reduced interdigitation in dense brush particle solids is provided in Figure 5d,e that depict TEM images of cracks formed approximately in monolayer films of intermediate (SiO_2-i-S1103, Figure 5d) and dense (SiO_2-d-S120, Figure 5e) brush particle systems with near equal organic content. Craze formation that was observed in sample SiO_2-i-S1103 provided evidence for the interdigitation of chains, while the smooth surface of cracks in the dense SiO_2-d-S120 system was indicative of brittle fracture (and hence the absence of significant chain entanglement). We note that the effect of graft architecture is expected to be reduced once the degree of polymerization is large enough to support sufficient brush interdigitation in dense systems; this is indeed consistent with the data shown in Figure 5a.

To further support the interpretation of the effect of graft architecture, an analytical model was used to estimate the role of brush interpenetration on the cohesive energy density and effective elastic modulus of brush particle films. Only van der Waals interactions between NP cores and London dispersion interactions between ligands were considered; the system was assumed to consist of silica NPs with uniform radius r_0 = 7.9 nm grafted with uniform PS chains of degree of polymerization N (i.e., particle and polymer molecular weight dispersity is neglected). van der Waals and ligand dispersion interactions in brush particle films were calculated on the basis of pairwise interaction models published in the literature.[71,72] Comparison between ligand–ligand and core–core interactions (see Figure S8) revealed that the latter is negligible if the distance between particle cores exceeds about 1 nm, which is small compared to the experimental value of particle spacings for any of the (intermediate or dense) brush systems that were the subject of the present study (see Figure 3). Hence, in the following, the contribution of core–core interactions to the cohesive interactions in dense and intermediate brush particle materials was neglected. Our approach consisted of two steps: first, the interparticle cohesive energy density (IPCED) was calculated such that it accounts (only) for the dispersion interactions contributed by chain segments that participate in interdigitation between adjacent brush particles (i.e., the interaction between ligands that are aligned end-on is neglected, see Figure 6a,b). The dispersion interaction between two side-on oriented ligands was determined from eq 1 that was first provided by Salem and later confirmed by numerous studies.

$$U_l(L) = -C_{PS}\frac{3\pi L}{8\lambda^2 x^5} \quad (1)$$

where $C_{PS} \approx 7.1 \times 10^{-79}$ J·m^6 is the interaction constant for PS, L is the length of overlap between two parallel (i.e., side-on aligned) chain segments, λ is the length of the monomer (~0.25 nm), and x is the intermolecular spacing between chains (~0.4 nm).[72−75] Note that we focused on the cohesive energy density contributed by interdigitating chain segments because it was expected to be the primary origin for the elastic forces resisting the perturbation of particle positions. In the second step, the effective elastic modulus was derived on the basis of the IPCED and compared with the experimental data.

https://dx.doi.org/10.1021/acs.macromol.9b01809
Macromolecules 2020, 53, 1502−1513

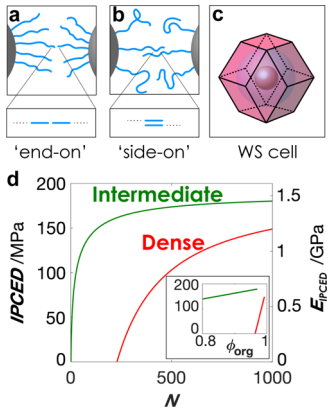

Figure 6. Illustrations of (a) end-on arrangement of densely tethered ligands and (b) side-on arrangement of interdigitated tethered ligands. The panel (c) shows a scheme of the WS cell of the particle brush (blue inner shell: CPB; red outer shell: SDPB). The panel (d) depicts a plot of IPCED in dense and intermediate brush particles as functions of degree of polymerization along with the corresponding values of elastic modulus (see the text for more detail). Inset shows IPCED as a function of organic volume fraction. The sign of IPCED was taken positive for convenience.

The IPCED was calculated as the sum of all dispersion interactions between interpenetrated ligands per material volume. To calculate IPCED, a cubic close-packed (face-centered cubic; fcc) microstructure of brush particle films was assumed.[2,42,50,56,76] The assumption of a lattice structure simplifies the estimation of the cohesive energy density because it reduces the relevant volume element to the respective Wigner−Seitz (WS) cell of the structure (e.g., a rhombic-dodecahedron in the case of fcc). Cubic close-packed structures have indeed been observed in films of dense brush particles and were rationalized as consequence of hard-sphere-type interactions between dense brush particles.[27,52,55] For brush systems with intermediate graft density (or dense systems with sufficiently high degree of polymerization of polymer tethers), the assumption of close packing is an approximation. However, because the errors associated with non-close packing were estimated to be within 15% of the result, fcc packing was assumed for all brush particle systems. Because the volume associated with each WS cell $V_{WS}(d) = (2r_0 + d)^3/\sqrt{2}$ is determined by the distance d between particle cores (d was known from TEM analysis, Figure 3) and because the volume fraction of the organic component was known from thermogravimetric analysis (TGA) characterization, the cohesive energy density of brush particle films could be estimated by summation of ligand dispersion interactions across each WS cell and subsequent normalization by the cell volume. To estimate the number of polymer repeat units contributing to the IPCED (i.e., the number of polymer repeat units that are part of interdigitating segments), the assumption was made that only segments in the SDPB regime participate in interdigitation. This restriction is motivated by prior reports demonstrating dense brush layers to allow for only limited overlap of polymer canopies both in the solution[50,73] and solid state.[8,9,32,55] For the dense brush particle series (SiO_2-d-SN), the CPB−SDPB transition was determined by evaluating the experimental scaling behavior $d \approx N^x$ (with x = 0.8 in the CPB and x = 0.5 in the SDPB regime, see Figure 3). Following this process, the IPCED could be expressed as

$$\mathrm{IPCED} = U_l(L)\frac{\lambda}{L}\rho_S\left[\frac{\sqrt{2}}{2}(2r_0 + BN^{0.5})^3 - \frac{4}{3}\pi\left(r_0 + \frac{A}{2}N_c^{0.8}\right)^3\right]\Big/\left[\frac{\sqrt{2}}{2}(2r_0 + BN^{0.5})^3\right] \quad (2)$$

where A = 0.335 nm and B = 0.907 nm are constants that are experimentally determined from Figure 3a, $L = N_{SDPB}\,\lambda$ is the length of side-on overlap among chains in the SDPB regime and $\rho_S = 6.07 \times 10^{27}$ m^{-3} is the number density of the repeat units (which was assumed to be independent of chain orientation). For brush systems with intermediate grafting density, the length of chain segments participating in interdigitation was assumed to be equal to the contour length of tethered chains. The resulting trend of IPCED for dense and intermediate brush particle systems is shown in Figure 6. The sign of IPCED was taken positive for convenience.

For materials undergoing only elastic−plastic deformation, the stored elastic energy upon deformation is directly related to the corresponding change in cohesive energy density (CED); the elastic modulus of brush particle films could be estimated from the calculated IPCED. Specifically, Willbourn demonstrated the empirical relation $E \simeq 8.04$ CED to apply to a wide range of polymers.[74] The resulting prediction of Young's moduli is depicted in Figure 6. Note that the predicted trend of E_{ICPED} confirmed the initial increase and following level-off with increasing degree of polymerization. Discrepancies from the experimental result might be attributable, in part, to the contribution of interparticle interaction between CPB-regime ligands to the total cohesive interaction, which is not considered in the calculation. Interestingly, despite the approximations made by the model, the resulting absolute values of the Young's modulus are captured within a factor of about two.

In contrast to dense and intermediate bush particle systems, sparse analogues displayed a systematic decrease of the elastic modulus with an increasing degree of polymerization of polymeric tethers, eventually levelling out at values of E corresponding to the reference homopolymer (see Figure 4). We attribute this opposing trend to the characteristic difference in microstructure in sparse brush particle films, specifically, the formation of string-like aggregate structures. As discussed above, van der Waals interactions between particle cores increase when particles are in close proximity (less than about 0.5 nm). This is also confirmed by recent molecular dynamics simulation by Midya et al. that have shown core interactions to dominate other interactions in sparse brush particle architectures.[45] Qualitatively, the increased core−core interactions enhance the IPCED of sparse brush materials and hence the elastic modulus. In fact, the mechanical properties of sparse brush particle hybrid materials might be better described by effective medium models for anisotropic filler shapes, such as the Cox short fiber model.[77] However, more quantitative information about the interactions within string aggregate structures would be required to test the applicability of effective medium models. Interestingly, the number of particles within aggregates (i.e., the string length) in SiO_2-s-SN systems decreases with an increasing degree of polymerization. The corresponding reduction of core−core contacts rationalizes the observed decrease of E with increasing N that is observed in SiO_2-s-SN systems. This situation is illustrated in Figure 7.

https://dx.doi.org/10.1021/acs.macromol.9b01809
Macromolecules 2020, 53, 1502−1513

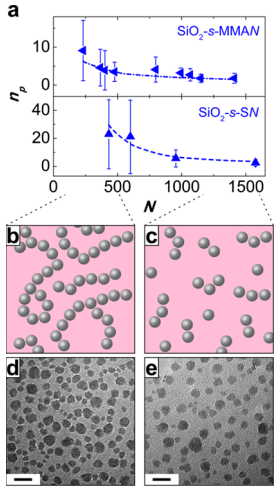

Figure 7. Structural transition in sparsely grafted particle films. The number of particles per string as a function of the degree of polymerization in PMMA analogue (top) and PS analogue (bottom) is plotted in a. Schematic illustrations of string formation in sparse brush particles when brushes are short (b) and long (c) are shown. The panel (d,e) shows corresponding electron micrographs for short- (d: SiO_2-s-S432) and long-tethered chains (e: SiO_2-s-S1576). Scale bars are 30 nm.

The aforementioned discussion centered on the interpretation of the elastic modulus of particle brush films. This was motivated by the direct relation between the cohesive energy density and the elastic modulus that enables the interpretation of modulus changes on the basis of the interactions between constituents. However, as explained above, the determination of elastic moduli from instrumented indentation experiments is subject to assumptions about parameters such as Poisson's ratio that are difficult to determine experimentally. A more directly accessible—but less readily interpretable—quantity is the material's hardness that directly follows from the peak loading during indentation. Figure 8 displays an Ashby chart correlating the elastic modulus and hardness for all tested brush materials.

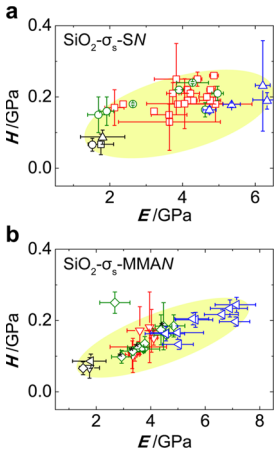

Figure 8. Indentation hardness (H) vs Young's modulus (E) plots of PS materials (a) and PMMA materials (b) (red: dense, green: intermediate, blue: sparse, black: initiator-tethered NPs; symbols are matched up with the corresponding system). Trends are highlighted in yellow.

The linear trend in the $E-H$ plots that is observed in the figure reveals that both quantities were correlated and hence obeyed similar structure−property relations. This supports the validity of the estimation of the Poisson ratio of particle brush materials on the basis of effective medium theory that was used to determine the elastic modulus of films (see Experimental Section). Figure 8 also might find use as "design guideline" for the synthesis of particle brush materials with desired properties. For high modulus and hardness, brush systems with reduced grafting density are clearly preferable, depending on the constraints on the targeted microstructure.

CONCLUSIONS

In this work, three series of brush particles were investigated, differentiated by grafting density as dense (∼1 nm^{-2}), intermediate (∼0.3 nm^{-2}), and sparse (∼0.05 nm^{-2}) brush systems. The density of tethered polymer chains exerted a pronounced effect on both structure and elastic modulus of films assembled from brush particles. Dense and intermediate systems displayed uniform microstructures, while sparse systems formed string-like superstructures. For dense and intermediate systems, the elastic modulus—measured through instrumented indentation analysis—increased with increasing degree of polymerization of tethered chains. At a given volume fraction of the organic component, the increase was found to be more pronounced for lower graft densities. This trend indicated that the restoring forces resisting elastic deformation are due to dispersion interactions between segments of interdigitated chains of adjacent brush particles. A reverse trend was observed in the case of materials that were assembled from sparse brush particles. Here, Young's modulus continuously decreased with increasing degree of polymerization of tethered chains—a trend that correlated with a decreasing number of particles per string.

We expect our results to be relevant in the context of mutual property optimization in particle brush-based hybrid materials. For example, if maximum reinforcement is to be achieved at high inorganic fractions and the formation of particle strings is to be avoided (such as in applications that require high dielectric breakdown strength), then, our results suggest that brush particles with intermediate grafting density can be advantageous. Open questions that warrant further investigation include the better understanding of the mechanism of reinforcement in the case of sparse particle brush assemblies. While the argument of increased contributions of core−core interactions is compelling, it is not clear why particle solids assembled from sparse initiator-capped particles (i.e., in the absence of any polymer) do not show a similar enhancement. We hypothesize that the lower modulus in the case of initiator-capped particles might be, in part, caused by void spaces in the microstructure that are not present in the case of polymer-tethered systems; however, this issue remains to be clarified. A second question relates to the role of experimental methodology. Complementary techniques such as Brillouin scattering (which probes the propagation of acoustic waves and hence gives information on both the bulk and the elastic modulus) could provide additional insights into the relevant modes of interaction in particle brush systems. An interesting question also concerns the role of chain length dispersity which was not considered in the present study. In particular, the deliberate control of the fraction of long to short chains could provide additional means to concurrently improve the modulus and

https://dx.doi.org/10.1021/acs.macromol.9b01809
Macromolecules 2020, 53, 1502−1513

fracture toughness of brush particle solids while maintaining a high inorganic content in the hybrid material.

EXPERIMENTAL SECTION

Materials. Monomers [styrene (S, 99%, Aldrich) and MMA (99%, Aldrich)] were purified by passing through a column filled with basic alumina to remove the inhibitor. Tris(2-dimethylaminoethyl)amine (Me_6TREN, 99%, Alfa), 4,4′-dinonyl-2,2′-bipyridyne (dNbpy, 97%, Aldrich), anisole (99%, Aldrich), tetrahydrofuran (THF, 99%, VWR), methanol (99%, VWR), hexane (99%, VWR), acetone (99%, VWR), *N*,*N*-dimethylformamide (DMF, 99%, VWR), 2-bromoisobutyryl bromide (2BiB, Aldrich, 98%), triethylamine (TEA, Aldrich, 99.5%), copper(II) bromide ($CuBr_2$, 99%, Aldrich), copper(II) chloride ($CuCl_2$, 99%, Aldrich), copper(I) chloride (CuCl, 97%, Sigma-Aldrich), tin(II) 2-ethylhexanoate ($Sn(EH)_2$, 95%, Aldrich), hexane (Fluka), 48% hydrofluoric acid aqueous solution (HF, >99.99%, Aldrich), ammonium hydroxide aqueous solution (NH_4OH, 28.0−30.0%, Fisher), anhydrous magnesium sulfate ($MgSO_4$, Fisher), and hexamethyldisilazane (HMDZ, Aldrich, 99%) were used as received unless otherwise stated. Copper(I) bromide (CuBr, 98%, Acros) was washed with glacial acetic acid to remove any soluble oxidized species, filtered, washed twice with anhydrous ethyl ether, dried, and kept in vacuum. Silica NPs (SiO_2) 30 wt % dispersion in methyl isobutyl ketone (MIBK-ST), with an effective radius of 7.9 ± 2.2 nm, measured by TEM, were donated by Nissan Chemical America Corp. The surface initiator densities are moderated with a dummy initiator chlorotrimethylsilane (99%, Aldrich).

Synthesis of Tetherable Initiator, 3-(Chlorodimethylsilyl)-propyl 2-Bromoisobutyrate (BiBSiCl). Allyl alcohol (18.6 mL, 273 mmol) and (TEA 38.1 mL, 273 mmol) were dissolved in 100 mL of dry THF in a round-bottom flask and cooled down to 0 °C in an ice bath; 27.0 (218 mmol) mL of 2BiB was diluted with 50 mL of dry THF. The 2BiB solution was added dropwise to the reaction solution over 30 min, while the reaction was stirred in the ice bath. The reaction mixture was then stirred at room temperature overnight. The resulting suspension was filtered, and the residue washed with THF. The filtrate was diluted with 200 mL of ethyl ether and washed three times with deionized water, once with saturated $NaHCO_3$ solution, and once with brine. The organic solution was dried over anhydrous Na_2SO_4. Upon removal of solvents in vacuo, allyl 2-bromoisobutyrate was obtained as a slightly yellow liquid. ^{1}H NMR (300 MHz, $CDCl_3$): δ 5.94 (dt, J = 17.3, 10.5, 5.6 Hz, 1H), 5.39 (dq, J = 17.3, 1.5 Hz, 1H), 5.27 (dq, J = 10.5, 1.5 Hz, 1H), 4.67 (dt, J = 5.5, 1.4 Hz, 2H), 1.95 (s, 6H) ppm.

Allyl 2-bromoisobutyrate (30.0 g, 145 mmol) and chlorodimethylsilane (94.4 mL, 869 mmol) were mixed in a round-bottom flask sealed with a rubber septum. The flask was placed in an ice bath, and dry nitrogen was bubbled through the solution for 10 min; 1.2 mL of Karstedt's catalyst solution was added dropwise to the purged solution; then, the reaction solution was stirred for two days after returning to room temperature. Conversion was monitored by ^{1}H NMR. Unreacted silane was removed by rotary evaporation. The platinum catalyst was precipitated when the crude product was cooled down to −18 °C and was removed via filtration through a 450 nm PTFE syringe filter. The product was obtained as a yellow liquid. ^{1}H NMR (300 MHz, $CDCl_3$) δ: 4.18 (t, J = 6.7 Hz, 2H), 1.94 (s, 6H), 1.86−1.78 (m, 2H), 0.93−0.83 (m, 2H), 0.44 (s, 6H) ppm.

Surface Modification of Silica NPs. Dry nitrogen was bubbled through 10 mL of a dispersion of the silica particles (in MIBK-ST) for 5 min; then, 1.5 mL of a mixture of initiator and dummy initiator solutions was slowly injected into the dispersion. The reaction was stirred at 60 °C for 24 h; then, the flask was cooled down to room temperature and 1.1 mL (5.4 mmol) of HMDZ was slowly injected to the reaction. The pale brown dispersion was stirred at 35 °C for another 12 h. The modified NPs were dialyzed against methanol three times and acetone twice.

SI-ATRP of PS-Grafted Silica NPs. Surface-modified NPs (SiO_2−Br), monomers (styrene, MMA), solvents (anisole, DMF), $CuBr_2$, and Me_6TREN were mixed thoroughly in a sealed Schlenk flask. Meanwhile, a stock solution of $Sn(EH)_2$ in anisole was prepared. Both mixtures were degassed by nitrogen purging; then, the $Sn(EH)_2$ solution was injected into the Schlenk flask to activate the catalyst complex, and the flask was immediately put into an oil bath. For a detailed procedure, we followed ref 4. Characteristics of the polymer were monitored by gravimetric analysis and size exclusion chromatography (SEC), respectively.

Size-Exclusion Chromatography. Number-average molecular weights (M_n) and MWDs were determined by SEC. The SEC was conducted with a Waters 515 pump and Waters 410 differential refractometer using PSS columns (Styrogel 105, 103, 102 Å) in THF as an eluent at 35 °C and at a flow rate of 1 mL min^{-1}. Linear PS and PMMA standards were used for calibration.

Thermogravimetric Analysis. TGA with TA Instruments 2950 was used to measure the fraction of SiO_2 in the hybrids. The data were analyzed with TA Universal Analysis. The heating procedure involved four steps: (1) jump to 120 °C; (2) hold at 120 °C for 10 min; (3) ramp up at a rate of 20 °C/min to 800 °C; and (4) hold for 2 min. The TGA plots were normalized to the total weight after holding at 120 °C.

Transmission Electron Microscopy. Approximately monolayer films of all particle brush systems were prepared by drop-casting of dilute colloidal solutions (∼ 1 mg/mL in THF) on a carbon-supported copper grid. The particulate film morphology and craze formation were studied using TEM with a JEOL EX2000 electron microscope operated at 200 kV. Images with amplitude and phase contrast were obtained by a Gatan Orius SC600 high-resolution camera.

Nanoindentation. Relatively thick films (>20 μm) were prepared from concentrated solutions (∼20 mg/mL) using PTFE molds. Elastic modulus and indentation hardness of films were characterized using an MTS nanoindenter XP with a Berkovich indenter of which the shape is tetrahedral. Displacement was under control to no more than 10% of the particulate film thickness to exclude any effect from substrates. Poisson's ratio of a material was calculated based on composition using the Voigt model for composite materials.[40] Details are shown in the Supporting Information. At least nine locations were indented with 500 nm depth limit, 5 nm/s displacement rate, 0.05 nm/s allowable drift rate, and 10 s constant loading time before unloading for each sample. The standard deviation of the measurements was calculated as the experimental error.

Atomic Force Microscopy. The residual indentations from nanoindentation were visualized using AFM on an NT-MDT Solver NEXT system in the semicontact mode with silicon cantilevers (300 kHz resonance frequency, 40 N m^{-1} force constant) of small tip radius (<10 nm). Samples were imaged in height and phase imaging modes to observe the indented surface.

Image Analysis. Micrographs were analyzed using the combination of ImageJ and MATLAB. Particle-to-particle distance was manually measured with ImageJ, while Voronoi tessellation analysis was carried out by programming with MATLAB. See details in the Supporting Information.

ASSOCIATED CONTENT

Supporting Information

The Supporting Information is available free of charge at https://pubs.acs.org/doi/10.1021/acs.macromol.9b01809.

Calculation of surface grafting density, calculation of Poisson's ratio of composite materials, additional material information, representative structure formation of the PMMA brush system, quantitative analysis of the domain structure using TEM micrographs, histograms of spacing between adjacent particle cores, representative load−displacement curves, and comparison of cohesive energy contributed from core−core interaction and ligand−ligand interaction (PDF)

https://dx.doi.org/10.1021/acs.macromol.9b01809
Macromolecules 2020, 53, 1502−1513

AUTHOR INFORMATION

Corresponding Author

Michael R. Bockstaller − *Department of Materials Science and Engineering, Carnegie Mellon University, Pittsburgh, Pennsylvania 15213, United States;* orcid.org/0000-0001-9046-9539; Email: bockstaller@cmu.edu

Authors

Jaejun Lee − *Department of Materials Science and Engineering, Carnegie Mellon University, Pittsburgh, Pennsylvania 15213, United States*

Zongyu Wang − *Department of Chemistry, Carnegie Mellon University, Pittsburgh, Pennsylvania 15213, United States*

Jianan Zhang − *Department of Materials Science and Engineering, Carnegie Mellon University, Pittsburgh, Pennsylvania 15213, United States; School of Chemistry and Chemical Engineering, Anhui University, Hefei 230601, China;* orcid.org/0000-0003-3195-9882

Jiajun Yan − *Department of Chemistry, Carnegie Mellon University, Pittsburgh, Pennsylvania 15213, United States;* orcid.org/0000-0003-3286-3268

Tingwei Deng − *Department of Materials Science and Engineering, Carnegie Mellon University, Pittsburgh, Pennsylvania 15213, United States*

Yuqi Zhao − *Department of Materials Science and Engineering, Carnegie Mellon University, Pittsburgh, Pennsylvania 15213, United States*

Krzysztof Matyjaszewski − *Department of Chemistry, Carnegie Mellon University, Pittsburgh, Pennsylvania 15213, United States;* orcid.org/0000-0003-1960-3402

Complete contact information is available at: https://pubs.acs.org/10.1021/acs.macromol.9b01809

Notes

The authors declare no competing financial interest.

ACKNOWLEDGMENTS

The financial support from the National Science Foundation (DMR 1501324, CMMI-1663305) and the Department of Energy (Basic Energy Sciences) via award DE-SC0018854 is gratefully acknowledged. The authors would like to further acknowledge use of facilities at the Materials Characterization Facility at Carnegie Mellon University under grant MCF-677785 and the Colloids, Surfaces, and Polymer Laboratory under grant CMU 678083-769798.

REFERENCES

(1) Emmerling, S. G. J.; Langer, L. B. N.; Pihan, S. A.; Lellig, P.; Gutmann, J. S. Patterning of a Surface Immobilized ATRP Initiator with an Inkjet Printer. *Macromolecules* **2010**, *43*, 5033−5042.

(2) Ohno, K.; Morinaga, T.; Takeno, S.; Tsujii, Y.; Fukuda, T. Suspensions of Silica Particles Grafted with Concentrated Polymer Brush: A New Family of Colloidal Crystals. *Macromolecules* **2006**, *39*, 1245−1249.

(3) Yan, J.; Pan, X.; Schmitt, M.; Wang, Z.; Bockstaller, M. R.; Matyjaszewski, K. Enhancing Initiation Efficiency in Metal-Free Surface-Initiated Atom Transfer Radical Polymerization (SI-ATRP). *ACS Macro Lett.* **2016**, *5*, 661−665.

(4) Pyun, J.; Matyjaszewski, K. Synthesis of Nanocomposite Organic/Inorganic Hybrid Materials Using Controlled/"Living" Radical Polymerization. *Chem. Mater.* **2001**, *13*, 3436−3448.

(5) Hui, C. M.; Pietrasik, J.; Schmitt, M.; Mahoney, C.; Choi, J.; Bockstaller, M. R.; Matyjaszewski, K. Surface-Initiated Polymerization as an Enabling Tool for Multifunctional (Nano-)Engineered Hybrid Materials. *Chem. Mater.* **2014**, *26*, 745−762.

(6) Barbey, R.; Lavanant, L.; Paripovic, D.; Schüwer, N.; Sugnaux, C.; Tugulu, S.; Klok, H.-A. Polymer Brushes via Surface-Initiated Controlled Radical Polymerization: Synthesis, Characterization, Properties, and Applications. *Chem. Rev.* **2009**, *109*, 5437−5527.

(7) Yan, J.; Bockstaller, M. R.; Matyjaszewski, K. Brush-Modified Materials: Control of Molecular Architecture, Assembly Behavior, Properties and Applications. *Prog. Polym. Sci.* **2019**, *100*, 101180.

(8) Choi, J.; Hui, C. M.; Pietrasik, J.; Dong, H.; Matyjaszewski, K.; Bockstaller, M. R.; Hui, M.; Pietrasik, J.; Dong, H.; Hui, C. M.; et al. Toughening Fragile Matter: Mechanical Properties of Particle Solids Assembled from Polymer-Grafted Hybrid Particles Synthesized by ATRP. *Soft Matter* **2012**, *8*, 4072.

(9) Schmitt, M.; Choi, J.; Min Hui, C.; Chen, B.; Korkmaz, E.; Yan, J.; Margel, S.; Burak Ozdoganlar, O.; Matyjaszewski, K.; Bockstaller, M. R. Processing Fragile Matter: Effect of Polymer Graft Modification on the Mechanical Properties and Processibility of (Nano-) Particulate Solids. *Soft Matter* **2016**, *12*, 3527−3537.

(10) Choi, J.; Dong, H.; Matyjaszewski, K.; Bockstaller, M. R. Flexible Particle Array Structures by Controlling Polymer Graft Architecture. *J. Am. Chem. Soc.* **2010**, *132*, 12537−12539.

(11) Tchoul, M. N.; Fillery, S. P.; Koerner, H.; Drummy, L. F.; Oyerokun, F. T.; Mirau, P. A.; Durstock, M. F.; Vaia, R. A. Assemblies of Titanium Dioxide-Polystyrene Hybrid Nanoparticles for Dielectric Applications. *Chem. Mater.* **2010**, *22*, 1749−1759.

(12) Huang, Y.; Zheng, Y.; Sarkar, A.; Xu, Y.; Stefik, M.; Benicewicz, B. C. Matrix-Free Polymer Nanocomposite Thermoplastic Elastomers. *Macromolecules* **2017**, *50*, 4742−4753.

(13) Bilchak, C. R.; Huang, Y.; Benicewicz, B. C.; Durning, C. J.; Kumar, S. K. High-Frequency Mechanical Behavior of Pure Polymer-Grafted Nanoparticle Constructs. *ACS Macro Lett.* **2019**, *8*, 294−298.

(14) Ginzburg, V. V. Modeling the Morphology and Phase Behavior of One-Component Polymer-Grafted Nanoparticle Systems. *Macromolecules* **2017**, *50*, 9445−9455.

(15) Hore, M. J. A. Polymers on nanoparticles: structure & dynamics. *Soft Matter* **2019**, *15*, 1120−1134.

(16) Fernandes, N. J.; Koerner, H.; Giannelis, E. P.; Vaia, R. A. Hairy Nanoparticle Assemblies as One-Component Functional Polymer Nanocomposites: Opportunities and Challenges. *MRS Commun.* **2013**, *3*, 13−29.

(17) Cang, Y.; Reuss, A. N.; Lee, J.; Yan, J.; Zhang, J.; Alonso-Redondo, E.; Sainidou, R.; Rembert, P.; Matyjaszewski, K.; Bockstaller, M. R.; et al. Thermomechanical Properties and Glass Dynamics of Polymer-Tethered Colloidal Particles and Films. *Macromolecules* **2017**, *50*, 8658−8669.

(18) Asai, M.; Cacciuto, A.; Kumar, S. K. Surface Fluctuations Dominate the Slow Glassy Dynamics of Polymer-Grafted Colloid Assemblies. *ACS Cent. Sci.* **2018**, *4*, 1179−1184.

(19) Zhang, Z.; Horsch, M. A.; Lamm, M. H.; Glotzer, S. C. Tethered Nano Building Blocks: Toward a Conceptual Framework for Nanoparticle Self-Assembly. *Nano Lett.* **2003**, *3*, 1341−1346.

(20) Ethier, J. G.; Hall, L. M. Structure and Entanglement Network of Model Polymer-Grafted Nanoparticle Monolayers. *Macromolecules* **2018**, *51*, 9878−9889.

(21) Ethier, J. G.; Hall, L. M. Modeling Individual and Pairs of Adsorbed Polymer-Grafted Nanoparticles: Structure and Entanglements. *Soft Matter* **2018**, *14*, 643−652.

(22) Hansoge, N. K.; Huang, T.; Sinko, R.; Xia, W.; Chen, W.; Keten, S. Materials by Design for Stiff and Tough Hairy Nanoparticle Assemblies. *ACS Nano* **2018**, *12*, 7946−7958.

(23) Kravchenko, V. S.; Potemkin, I. I. Self-Assembly of Rarely Polymer-Grafted Nanoparticles in Dilute Solutions and on a Surface: From Non-Spherical Vesicles to Graphene-like Sheets. *Polymer* **2018**, *142*, 23−32.

(24) Jiao, Y.; Tibbits, A.; Gillman, A.; Hsiao, M.-S.; Buskohl, P.; Drummy, L. F.; Vaia, R. A. Deformation Behavior of Polystyrene-Grafted Nanoparticle Assemblies with Low Grafting Density. *Macromolecules* **2018**, *51*, 7257−7265.

(25) Mahoney, C.; Hui, C. M.; Majumdar, S.; Wang, Z.; Malen, J. A.; Tchoul, M. N.; Matyjaszewski, K.; Bockstaller, M. R. Enhancing Thermal Transport in Nanocomposites by Polymer-Graft Modification of Particle Fillers. *Polymer* **2016**, *93*, 72−77.
(26) Grabowski, C. A.; Koerner, H.; Meth, J. S.; Dang, A.; Hui, C. M.; Matyjaszewski, K.; Bockstaller, M. R.; Durstock, M. F.; Vaia, R. A. Performance of Dielectric Nanocomposites: Matrix-Free, Hairy Nanoparticle Assemblies and Amorphous Polymer-Nanoparticle Blends. *ACS Appl. Mater. Interfaces* **2014**, *6*, 21500−21509.
(27) Alonso-Redondo, E.; Schmitt, M.; Urbach, Z.; Hui, C. M.; Sainidou, R.; Rembert, P.; Matyjaszewski, K.; Bockstaller, M. R.; Fytas, G. A New Class of Tunable Hypersonic Phononic Crystals Based on Polymer-Tethered Colloids. *Nat. Commun.* **2015**, *6*, 8309.
(28) Wang, Z.; Lu, Z.; Mahoney, C.; Yan, J.; Ferebee, R.; Luo, D.; Matyjaszewski, K.; Bockstaller, M. R. Transparent and High Refractive Index Thermoplastic Polymer Glasses Using Evaporative Ligand Exchange of Hybrid Particle Fillers. *ACS Appl. Mater. Interfaces* **2017**, *9*, 7515−7522.
(29) Yan, J.; Malakooti, M. H.; Lu, Z.; Wang, Z.; Kazem, N.; Pan, C.; Bockstaller, M. R.; Majidi, C.; Matyjaszewski, K. Solution Processable Liquid Metal Nanodroplets by Surface-Initiated Atom Transfer Radical Polymerization. *Nat. Nanotechnol.* **2019**, *14*, 684−690.
(30) Mbanga, B. L.; Iyer, B. V. S.; Yashin, V. V.; Balazs, A. C. Tuning the Mechanical Properties of Polymer-Grafted Nanoparticle Networks through the Use of Biomimetic Catch Bonds. *Macromolecules* **2016**, *49*, 1353−1361.
(31) Bilchak, C. R.; Buenning, E.; Asai, M.; Zhang, K.; Durning, C. J.; Kumar, S. K.; Huang, Y.; Benicewicz, B. C.; Gidley, D. W.; Cheng, S.; et al. Polymer-Grafted Nanoparticle Membranes with Controllable Free Volume. *Macromolecules* **2017**, *50*, 7111−7120.
(32) Akcora, P.; Liu, H.; Kumar, S. K.; Moll, J.; Li, Y.; Benicewicz, B. C.; Schadler, L. S.; Acehan, D.; Panagiotopoulos, A. Z.; Pryamitsyn, V.; et al. Anisotropic Self-Assembly of Spherical Polymer-Grafted Nanoparticles. *Nat. Mater.* **2009**, *8*, 354−359.
(33) Jiao, Y.; Akcora, P. Assembly of Polymer-Grafted Magnetic Nanoparticles in Polymer Melts. *Macromolecules* **2012**, *45*, 3463−3470.
(34) Liu, S.; Senses, E.; Jiao, Y.; Narayanan, S.; Akcora, P. Structure and Entanglement Factors on Dynamics of Polymer-Grafted Nanoparticles. *ACS Macro Lett.* **2016**, *5*, 569−573.
(35) Bianchi, E.; Blaak, R.; Likos, C. N. Patchy Colloids: State of the Art and Perspectives. *Phys. Chem. Chem. Phys.* **2011**, *13*, 6397−6410.
(36) Chao, H.; Riggleman, R. A. Inverse Design of Grafted Nanoparticles for Targeted Self-Assembly. *Mol. Syst. Des. Eng.* **2018**, *3*, 214−222.
(37) Phillips, C. L.; Glotzer, S. C. Effect of Nanoparticle Polydispersity on the Self-Assembly of Polymer Tethered Nanospheres. *J. Chem. Phys.* **2012**, *137*, 104901.
(38) Marson, R. L.; Nguyen, T. D.; Glotzer, S. C. Rational Design of Nanomaterials from Assembly and Reconfigurability of Polymer-Tethered Nanoparticles. *MRS Commun.* **2015**, *5*, 397−406.
(39) Nielsen, L. E.; Landel, R. F. *Mechanical Properties of Polymers and Composites*; CRC Press, 1994.
(40) Ward, I. M.; Sweeney, J. *An Introduction to the Mechanical Properties of Solid Polymers*, 2nd ed.; Wiley, 2004.
(41) Tobolsky, A. V. *Properties and Structure of Polymers*; Wiley, 1960.
(42) Podsiadlo, P.; Krylova, G.; Lee, B.; Critchley, K.; Gosztola, D. J.; Talapin, D. V.; Ashby, P. D.; Shevchenko, E. V. The Role of Order, Nanocrystal Size, and Capping Ligands in the Collective Mechanical Response of Three-Dimensional Nanocrystal Solids. *J. Am. Chem. Soc.* **2010**, *132*, 8953−8960.
(43) Gu, X. W.; Ye, X.; Koshy, D. M.; Vachhani, S.; Hosemann, P.; Alivisatos, A. P. Tolerance to Structural Disorder and Tunable Mechanical Behavior in Self-Assembled Superlattices of Polymer-Grafted Nanocrystals. *Proc. Natl. Acad. Sci. U.S A.* **2017**, *114*, 2836−2841.
(44) Hilburg, S. L.; Elder, A. N.; Chung, H.; Ferebee, R. L.; Bockstaller, M. R.; Washburn, N. R. A Universal Route towards Thermoplastic Lignin Composites with Improved Mechanical Properties. *Polymer* **2014**, *55*, 995−1003.
(45) Midya, J.; Cang, Y.; Egorov, S. A.; Matyjaszewski, K.; Bockstaller, M. R.; Nikoubashman, A.; Fytas, G. Disentangling the Role of Chain Conformation on the Mechanics of Polymer Tethered Particle Materials. *Nano Lett.* **2019**, *19*, 2715−2722.
(46) Giovino, M.; Pribyl, J.; Benicewicz, B.; Bucinell, R.; Schadler, L. Mechanical Properties of Polymer Grafted Nanoparticle Composites. *Nanocomposites* **2018**, *4*, 244−252.
(47) Choi, J.; Hui, C. M.; Schmitt, M.; Pietrasik, J.; Margel, S.; Matyjazsewski, K.; Bockstaller, M. R. Effect of Polymer-Graft Modification on the Order Formation in Particle Assembly Structures. *Langmuir* **2013**, *29*, 6452−6459.
(48) Askar, S.; Li, L.; Torkelson, J. M. Polystyrene-Grafted Silica Nanoparticles: Investigating the Molecular Weight Dependence of Glass Transition and Fragility Behavior. *Macromolecules* **2017**, *50*, 1589−1598.
(49) Daoud, M.; Cotton, J. P. Star shaped polymers : a model for the conformation and its concentration dependence. *J. Phys.* **1982**, *43*, 531−538.
(50) Ohno, K.; Morinaga, T.; Takeno, S.; Tsujii, Y.; Fukuda, T. Suspensions of Silica Particles Grafted with Concentrated Polymer Brush: Effects of Graft Chain Length on Brush Layer Thickness and Colloidal Crystallization. *Macromolecules* **2007**, *40*, 9143−9150.
(51) Mongcopa, K. I. S.; Poling-Skutvik, R.; Ashkar, R.; Butler, P.; Krishnamoorti, R. Conformational Change and Suppression of the Θ -Temperature for Solutions of Polymer-Grafted Nanoparticles. *Soft Matter* **2018**, *14*, 6102−6108.
(52) Chen, J.; Fasoli, A.; Cushen, J. D.; Wan, L.; Ruiz, R. Self-Assembly and Directed Assembly of Polymer Grafted Nanocrystals via Solvent Annealing. *Macromolecules* **2017**, *50*, 9636−9646.
(53) Ohno, K.; Morinaga, T.; Koh, K.; Tsujii, Y.; Fukuda, T. Synthesis of Monodisperse Silica Particles Coated with Well-Defined, High-Density Polymer Brushes by Surface-Initiated Atom Transfer Radical Polymerization. *Macromolecules* **2005**, *38*, 2137−2142.
(54) Wang, Z.; Yan, J.; Liu, T.; Wei, Q.; Li, S.; Olszewski, M.; Wu, J.; Sobieski, J.; Fantin, M.; Bockstaller, M. R.; et al. Control of Dispersity and Grafting Density of Particle Brushes by Variation of ATRP Catalyst Concentration. *ACS Macro Lett.* **2019**, *8*, 859−864.
(55) Voudouris, P.; Choi, J.; Dong, H.; Bockstaller, M. R.; Matyjaszewski, K.; Fytas, G. Effect of Shell Architecture on the Static and Dynamic Properties of Polymer-Coated Particles in Solution. *Macromolecules* **2009**, *42*, 2721−2728.
(56) Morinaga, T.; Ohno, K.; Tsujii, Y.; Fukuda, T. Structural Analysis of "Semisoft" Colloidal Crystals by Confocal Laser Scanning Microscopy. *Macromolecules* **2008**, *41*, 3620−3626.
(57) Ohno, K.; Koh, K.; Tsujii, Y.; Fukuda, T. Fabrication of Ordered Arrays of Gold Nanoparticles Coated with High-Density Polymer Brushes. *Angew. Chem., Int. Ed.* **2003**, *42*, 2751−2754.
(58) Nakanishi, Y.; Ishige, R.; Ogawa, H.; Sakakibara, K.; Ohno, K.; Morinaga, T.; Sato, T.; Kanaya, T.; Tsujii, Y. USAXS Analysis of Concentration-Dependent Self-Assembling of Polymer-Brush-Modified Nanoparticles in Ionic Liquid: [I] Concentrated-Brush Regime. *J. Chem. Phys.* **2018**, *148*, 124902.
(59) Bachhar, N.; Jiao, Y.; Asai, M.; Akcora, P.; Bandyopadhyaya, R.; Kumar, S. K. Impact of the Distributions of Core Size and Grafting Density on the Self-Assembly of Polymer Grafted Nanoparticles. *Macromolecules* **2017**, *50*, 7730−7738.
(60) Hickey, R. J.; Seo, M.; Luo, Q.; Park, S.-J. Directional Self-Assembly of Ligand-Stabilized Gold Nanoparticles into Hollow Vesicles through Dynamic Ligand Rearrangement. *Langmuir* **2015**, *31*, 4299−4304.
(61) Hakem, I. F.; Leech, A. M.; Johnson, J. D.; Donahue, S. J.; Walker, J. P.; Bockstaller, M. R. Understanding Ligand Distributions in Modified Particle and Particlelike Systems. *J. Am. Chem. Soc.* **2010**, *132*, 16593−16598.
(62) Choi, J.; Hore, M. J. A.; Clarke, N.; Winey, K. I.; Composto, R. J. Nanoparticle Brush Architecture Controls Polymer Diffusion in Nanocomposites. *Macromolecules* **2014**, *47*, 2404−2410.

https://dx.doi.org/10.1021/acs.macromol.9b01809
Macromolecules 2020, 53, 1502−1513

(63) Chevigny, C.; Gigmes, D.; Bertin, D.; Jestin, J.; Boué, F. Polystyrene Grafting from Silica Nanoparticles via Nitroxide-Mediated Polymerization (NMP): Synthesis and SANS Analysis with the Contrast Variation Method. *Soft Matter* **2009**, *5*, 3741−3753.
(64) Choi, J.; Hore, M. J. A.; Meth, J. S.; Clarke, N.; Winey, K. I.; Composto, R. J. Universal Scaling of Polymer Diffusion in Nanocomposites. *ACS Macro Lett.* **2013**, *2*, 485−490.
(65) Gam, S.; Meth, J. S.; Zane, S. G.; Chi, C.; Wood, B. A.; Winey, K. I.; Clarke, N.; Composto, R. J. Polymer Diffusion in a Polymer Nanocomposite: Effect of Nanoparticle Size and Polydispersity. *Soft Matter* **2012**, *8*, 6512−6520.
(66) Oliver, W. C.; Pharr, G. M. Measurement of Hardness and Elastic Modulus by Instrumented Indentation: Advances in Understanding and Refinements to Methodology. *J. Mater. Res.* **2004**, *19*, 3−20.
(67) Avice, J.; Boscher, C.; Vaudel, G.; Brotons, G.; Juvé, V.; Edely, M.; Méthivier, C.; Gusev, V. E.; Belleville, P.; Piombini, H.; et al. Controlling the Nanocontact Nature and the Mechanical Properties of a Silica Nanoparticle Assembly. *J. Phys. Chem. C* **2017**, *121*, 23769−23776.
(68) Griesemer, S. D.; You, S. S.; Kanjanaboos, P.; Calabro, M.; Jaeger, H. M.; Rice, S. A.; Lin, B. The Role of Ligands in the Mechanical Properties of Langmuir Nanoparticle Films. *Soft Matter* **2017**, *13*, 3125−3133.
(69) Guth, E. Theory of Filler Reinforcement. *J. Appl. Phys.* **1945**, *16*, 20−25.
(70) Ghosh, S. K.; Cherstvy, A. G.; Petrov, E. P.; Metzler, R. Interactions of Rod-like Particles on Responsive Elastic Sheets. *Soft Matter* **2016**, *12*, 7908−7919.
(71) Israelachvili, J. *Intermolecular and Surface Forces*, 3rd ed.; Academic Press, 2011.
(72) Salem, L. Attractive Forces between Long Saturated Chains at Short Distances. *J. Chem. Phys.* **1962**, *37*, 2100.
(73) Boles, M. A.; Talapin, D. V. Many-Body Effects in Nanocrystal Superlattices: Departure from Sphere Packing Explains Stability of Binary Phases. *J. Am. Chem. Soc.* **2015**, *137*, 4494−4502.
(74) Willbourn, A. H. Molecular Design of Polymers. *Polymer* **1976**, *17*, 965−976.
(75) Gedde, U. W. *Polymer Physics*; Springer Science & Business Media, 1995.
(76) Zhang, H.; Wang, W.; Akinc, M.; Mallapragada, S.; Travesset, A.; Vaknin, D. Assembling and Ordering Polymer-Grafted Nanoparticles in Three Dimensions. *Nanoscale* **2017**, *9*, 8710−8715.
(77) Cox, H. L. The Elasticity and Strength of Paper and Other Fibrous Materials. *Br. J. Appl. Phys.* **1952**, *3*, 72−79.

https://dx.doi.org/10.1021/acs.macromol.9b01809
Macromolecules 2020, 53, 1502−1513